Review of Scientific Instruments

RESEARCH ARTICLE | DECEMBER 13 2022

Design and construction of a novel energy-loss optical scintillation system (ELOSS) for heavy-ion particle identification

M. Cortesi ; S. Dziubinski ; A. Gade ; R. Zegers ; J. Pereira; J. Asciutto; S. Lidia ; D. Bazin

Rev Sci Instrum 93, 123305 (2022)
https://doi.org/10.1063/5.0124846

AIP Publishing

Review of Scientific Instruments ARTICLE scitation.org/journal/rsi

Design and construction of a novel energy-loss optical scintillation system (ELOSS) for heavy-ion particle identification

Cite as: Rev. Sci. Instrum. 93, 123305 (2022); doi: 10.1063/5.0124846
Submitted: 8 September 2022 • Accepted: 18 November 2022 •
Published Online: 13 December 2022

M. Cortesi,[1,a] S. Dziubinski,[1,2] A. Gade,[1,2] R. Zegers,[1,2] J. Pereira,[1] J. Asciutto,[1] S. Lidia,[1] and D. Bazin[1,2]

AFFILIATIONS

[1] Facility for Rare Isotope Beams, Michigan State University, East Lansing, Michigan 48824, USA
[2] Department of Physics and Astronomy, Michigan State University, East Lansing, Michigan 48824, USA

[a] Author to whom correspondence should be addressed: cortesi@frib.msu.edu

ABSTRACT

We present the development of a novel heavy-ion particle-identification (PID) device based on an energy-loss measurement to be implemented in the focal plane of the S800 spectrograph of the Facility for Rare Isotope Beams (FRIB). The new instrument consists of a multi-segmented optical detector [energy-loss optical scintillation system (ELOSS)] that is filled with xenon at pressures ranging from 400 to 800 Torr. The gas volume is surrounded by arrays of photomultiplier tubes and placed along the direction of the beam for recording the prompt scintillation light. The number of detected photons, which is proportional to the energy deposited by the beam particle along its track in the detector volume, allows one to identify the corresponding atomic number (Z). The ELOSS technology is expected to provide high-resolution ΔE measurements (≤0.6% σ) at a high counting rate (>50 kHz). In addition, it has the capability of providing timing information with around 150 ps resolution (σ) compared to the lack of useable timing information of the conventional ionization chamber relying on drifting charges. The development of fast, accurate ΔE measurement techniques for present and future nuclear science facilities will have a high impact on the design and implementation of rare-isotope beam experiments at FRIB and their scientific outcome. As such, ELOSS also represents a prototype for the development of PID detector systems of other planned and future spectrometers, such as the high rigidity spectrometer at FRIB.

I. INTRODUCTION

The S800 superconducting spectrograph at the Facility for Rare Isotope Beams (FRIB)[1] is used for experiments using radioactive beams produced by projectile fragmentation. It is characterized by a large total momentum acceptance (±3% in focus mode) and a maximum magnetic rigidity of up to 4 Tm. The heavy-ion particle identification (PID) in the focal plane of the S800 spectrograph is based on the TOF-Bρ-ΔE method in which the simultaneous measurement of the energy loss (ΔE), the velocity via time of flight (TOF), and magnetic rigidity (Bρ) are used to deduce the atomic number (Z) and the mass-to-charge ratio (A/Q) of magnetically separated projectile-like reaction residues.[2,3] The additional measurement of the total energy (E) allows A and Q to be determined independently, which enables charge-state identification. To separate the reaction products entering the focal plane according to their proton number Z, the energy-loss measurement requires good energy resolution (<1% σ),[4] a low material budget (25–30 mg/cm^2), a homogeneous coverage for a uniform detector response across the full active area, a high counting rate capability (>20 kHz), and radiation hardness.

The energy-loss measurement at the focal plane of the S800 spectrograph is presently performed using a conventional grid-less, multi-segmented ionization chamber (IC).[5] The detector is filled with P10 gas at a typical pressure of 300 Torr, although the pressure can be increased up to 600 Torr for light nuclei. The IC consists of 16 stacked-parallel plate ionization chambers that are placed along the detector's central axis and perpendicular to the beam direction. Thin anode–cathode foils, separated by a 3 cm gas gap, bound the extent of the individual IC section. Incident beam particles that pass

through the thin gas gap between the electrode foils ionize the gas molecules along their trajectories. The ionization electrons and the positive ions drift away in opposite directions and are collected on the IC electrode foils. The mean energy deposition measured in the detector is then proportional to the square of the atomic number (Z) of the impinging particle.

This grid-less "anode–cathode" configuration allows ionization electrons and ions to be collected over a very short distance, resulting in an effective reduction of a pile-up. However, the signals have position-dependent pulse shapes, making it difficult to determine the ΔE-values uniformly between the short gas gaps. In addition, the large surface area of the electrode foil leads to a high detector capacitance, resulting in considerable electronic noise that degrades the signal-to-noise ratio and thus limits the energy resolution. To avoid the position-dependent pulse shapes of the grid-less ICs, Frisch-grid configurations can be used instead,[6] but at the expense of count rate capability due to the long charge collection time. Both the grid-less IC and the Frisch-grid IC have typical energy resolutions limited to around a few percent, which corresponds to a reduced resolving power, of about $\Delta Z/Z = 0.4–0.5$ for nuclei up to $Z = 50$ (Sn). Secondary effects, which include delta electrons (created by the heavy ions that impact the entrance window), and attachment (during the drift of the ionization electrons in the gas medium), significantly deteriorate the charge resolving power at high Z. With the present IC design and technology, from a practical standpoint, reasonable energy resolutions (of around 1%) are achieved only for nuclei with $Z < 50$.

The unprecedented discovery potential of a modern rare isotope beam facility, such as FRIB, can only be realized by implementing state-of-the-art experimental equipment capable of studying these isotopes at high beam rates and optimal resolutions. This work reports the progress on the design and construction of advanced, innovative instrumentation for the highly accurate and efficient identification of the atomic number (Z) of nuclei transmitted to the focal plane of high-resolution magnetic spectrographs. The detector concept is based on event-by-event Energy-Loss measurement in a multi-segmented Optical Scintillator System (ELOSS), which records the scintillation light produced by a charged particle traveling through a high-scintillation gas. We discuss the optimization of the optical readout configuration based on Vacuum Ultra-Violet (VUV)-sensitive PhotoMultiplier Tubes (PMTs), the expected performance of the novel detector concept, and the overall impact on radiation-detection physics and technology applied to the field of experimental nuclear physics with heavy-ion beams. The fabrication and test of the ELOSS components, including interfaces and data acquisition system (DAQ), will be completed by early 2023. The detector will be installed into the S800 focal plane detector system and commissioned by September 2023.

II. THE ENERGY-LOSS OPTICAL SCINTILLATOR SYSTEM (ELOSS)

The basic scheme and concept of the ELOSS detector are depicted in Fig. 1. ELOSS has a rectangular active area of 30×60 cm^2, which matches the size of the other S800 focal plane detectors (e.g., the tracking detectors[7]), and an effective thickness of 19 cm. The ELOSS vessel is a large stainless-steel chamber filled with pure xenon. The pressure of the gas can be adjusted from 400 to

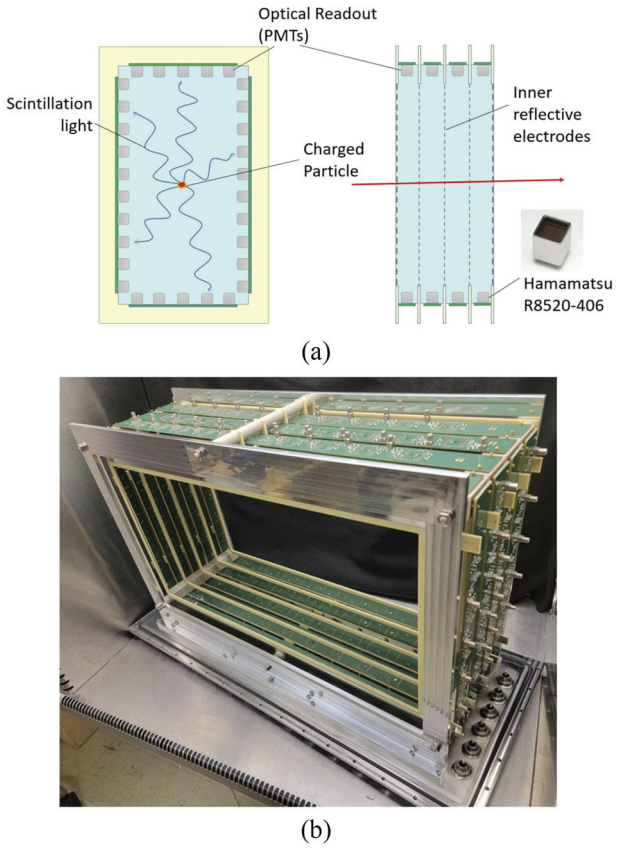

FIG. 1. Schematic drawing of the ELOSS detector concept (a) and photographs of the ELOSS optical readout assembly (with no PMTs) including mechanical supports (b).

800 Torr, depending on the mass, charge, and energy of the reaction products to be detected.

The detector's effective volume is segmented into four sectors along the beam direction, each of which is 47 mm wide. Arrays of uniformly spaced PhotoMultipliers Tube (PMTs) are positioned at the four sides of each sector and serve as an optical readout for recording the prompt Xe scintillation light. Each sector comprises a total of 30 PMTs [Fig. 1(a)] with a high sensitivity to the Xe light emission (peaked at 178 nm).[8] Metalized polypropylene foils (0.75 μm thick) separate the sectors from each other. The foils have a 150 nm thick Al layer evaporated on both surfaces, which reflects and guides the Xe scintillation light toward the PMT arrays. The estimated reflectivity of the Al-evaporated foils is >80%.[9] The foils can be optionally biased to create a suitable electric field in the Xe-filled gap to stimulate light emission via the electroluminescence process. The foils are held by Printed Circuit Board (PCB) frames, which also host the electrical connection for delivering the bias voltages.

The vessel is equipped with an entrance and an exit pressure window made of poly(*p*-phenylene terephthalamide) (PPTA) foil, reinforced by an overlay of Kevlar plain weave fabric (FG-KEV1738 38 in. KEVLAR®), and sealed with epoxy (Fiberglast system 2000

2-part laminating epoxy resin[10]). The foils are fastened to an aluminum frame with epoxy (Hexion EPON 828[11]). The pressure window has a total thickness of around 14 mg/cm^2 and is designed to withstand a maximum differential pressure of up to 1.3 atm with a marginal energy-loss and angular straggling on the impinging charged particles. The Al frame also hosts the gas fittings for the connection to the gas handling system (GHS), as well as the bypass valve that opens to the focal plane chamber to vent and evacuate the detector.

When a charged particle traverses the detector volume, it undergoes collisions with Xe atoms to produce inelastic phenomena, excitation of various kinds, and ionization. With no electric field applied across the gas volume, the electron–ion pairs recombine immediately. The Xe are left in an excited state either by the recombination process or directly by the inelastic collision with the impinging charged particle. They form exicted dimers that return to the ground state through single or multiple transitions, which result in a large photon-emission with a characteristic peak at 178 nm.[8] The metalized parallel foils that separate the various detector compartments, driving the photon toward the optical readout at the detector volume edges, reflect the scintillation light created in each sector. This results in an enhanced photon-collection efficiency.

An even larger amount of light may be produced when a suitable electric field is applied between the metalized, parallel-plate electrodes that confine the Xe gas volume of each sector. Under this condition, the ionization electrons released along the trajectory of the heavy-ion do not recombine, but they are instead following the electric field lines similar to a conventional gridless ionization chamber.[12,13] The voltage difference between the electrodes can be tuned to allow the primary electrons to excite other Xe atoms without producing a further avalanche. This corresponds to operating the parallel-plate compartments at electric field strengths near the upper end of the ionization region, enabling extremely good energy–light correlation and thus excellent energy resolution.[14]

Unlike the conventional ionization chambers based on ionization charge readout, the ELOSS detector measures the energy deposited in the gas by recording the primary and stimulated scintillation light. The amount of energy loss in the gas by the impinging charged particle is proportional to the total number of photons recorded by the optical readout. The proportionality constant takes into account the photon detection efficiency of the photo-sensors, the solid angle subtended by the optical readout, the photon collection efficiency, and the primary (or stimulated) scintillation yield of the Xe gas. The photon detection efficiency of each PMT will be measured by comparing its responsivity with respect to the one of a calibrated photodiode—namely, a photodiode whose spectral responsivity is calibrated at a photo-current level of pico-Ampere. The solid angle seen by the optical readout and the photon collection efficiency can be both accurately estimated using GEANT4 Monte Carlo simulations. The modeling of the detector will take into account all of the relevant parameters, including the reflection/absorption efficiency of the reflecting Al foils, the geometry of the ELOSS detector (i.e., the thickness of the sector), the number of PMTs, and the size of the sensitive photocathode area of the PMT. The scintillation yield of the Xe gas for heavy ions presents the largest uncertainty, as the scintillation yield depends on the Linear Energy Transfer (LET), and very little data are available in the literature for heavy ions with energy ranging from 50–150 MeV/u. For the above reason, the ELOSS commissioning at the S800 spectrometer focal plane will include an energy calibration measurement. During this, the energy deposited in the Xe effective volume will be accurately correlated with the light recorded by the ELOSS optical readout, and the corresponding energy resolution will be extracted. This will be achieved by computing the energy of the beam particles impinging on the ELOSS from the measurement of the magnetic rigidity on an event-by-event basis and by measuring the residual kinetic energy after ELOSS using the CsI(Na) hodoscope. The energy loss by the beam particles in the passive elements of ELOSS (pressure windows, electrode foils, etc.) will be also estimated and taken into consideration, by comparing the residual total kinetic energy measured by the CsI(Na) hodoscope with and without the Xe gas filling ELOSS.

A. The optical readout and interfaces

The full optical readout consists of 120 Hamamatsu 1-in. 10-stage PMTs, model R8520-406,[15] rated for operation at temperatures ranging from −110 to +50 °C, and pressures up to 5 atm. The selected number of PMTs and their arrangement in the arrays allow for a high light collection efficiency combined with a low-cost readout solution, the latter consisting of the minimal number of PMTs and associated electronics [high-voltage (HV) and DAQ channels].

The Hamamatsu R8520-406 PMT is equipped with a UV glass entrance window and a Bialkali-LT photocathode, which is characterized by a spectral response in the range of 160–650 nm and a quantum efficiency of around 35% at 178 nm.[16] The typical pulse rise time is about 1.8 ns for a single photoelectron. Each PMT is instrumented with a positive high-voltage (HV) divider circuit that is mounted on a custom-built Printed Circuit Board (PCB). The PCB also serves as a mechanical support for the PMTs. The PMTs are held in position by the pin-socket connections on the bottom side and fastened with machined Al bars that rest on the edge of the PMT glass window, acting as a clamp on the top side.

The HV biases and signals that are routed out via Kapton-insulated, miniature coaxial cables were terminated with the LEMO connector (model L00) on the voltage-divider PCB side and with the sub-D 25 pin connectors (Allectra model 218-D25-SS-1KV) on the flange side. The mechanical supports for the voltage-divider of the PMTs, the support of the frames of the reflective foils, and the sub-D HV/signals feedthrough are all fastened to the ELOSS vessel lid, allowing easy and fast service access to the detector. All the non-metallic mechanical components installed in the inner detector volume are made out of low-outgassing PEEK material,[17] in order to reduce the amount of impurities in the Xe and preserve a high scintillation yield.

The PMTs are biased with a positive HV voltage configuration (typically 800 V), where the photocathode is at the ground. This technical solution also allows one to achieve the highest single photoelectron resolution, and it reduces any potential interference with the electric field in the gas gap when the electrode foils are also biased.

The design of the voltage-divider circuitry is based on the recommendations provided on the Hamamatsu R8520-406 datasheet.[15]

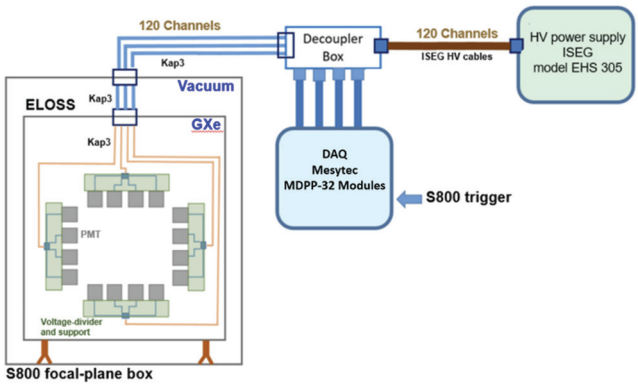

FIG. 2. Schematic drawing of the ELOSS detector interfaces.

The total resistance of the full voltage-divider chain is chosen to be 5 MΩ, with the aim of maximizing rate, preserving good linearity, and avoiding excessive current running through the circuitry, which may cause undesired heat and thermal side-effects on the passive elements. The base is back-terminated with a 2 kΩ resistor, which increases the charge collection at the output and minimizes signal distortion.

In order to optimize the uniformity of the optical readout response and achieve the best energy resolution, only carefully selected PMTs with an anode sensitivity ranging from 100 to 800 A/lm have been employed in the setup (typical sensitivity of the R8520-406 may vary from 10 to 1000 A/lm[18]). In addition, the PMT's anode sensitivities are further corrected by adjusting the potential ratio of two consecutive center-stage dynodes on the voltage-diver PCB of each device and finally by fine-tuning the supply voltages. The PMT's calibration procedure and the correction of the anode sensitivities are reported elsewhere.[19]

A decoupler box, placed outside the S800 focal plane chamber, is used to deliver the bias voltage to the PMTs and the capacity pickup of the PMT's signals. This minimizes the number of cables and feedthroughs (Fig. 2) from the focal plane chamber to the ELOSS detector, which is a very similar technical solution developed for the PandaX project.[20] The decoupler box circuitry includes a low-pass filter installed on each HV channel, which filters out the high-frequency noise generated by the HV power supply, and an AC capacitor (10 nF). The voltages for the PMTs and the electrode foils are supplied by an ISEG HV system using a Mpod EC main frame and three EHS 305 modules (48 HV channels up to 3 kV and 1 mA). The electrical connection between the ISEG HV modules and the decoupler box is performed via 48 channel multi-wire cables equipped with REDEL connectors on both ends.

B. The gas handling system

The ELOSS Gas Handling System (GHS) is designed to fill, regulate, and empty the detector volume. The main components of the GHS include a gas-bottle rack with a pressure regulator for the injection of the Xe gas into the system, a purification system for the online removal of impurities, a control system for the regulation of the gas flow, and a Xe gas recovery/storage system. A schematic drawing of the gas handling system is shown in Fig. 3.

The Xe recovery system consists of a single-ended sampling cylinder (FAV, model FSCS3225012N10) rated at 10 000 PSI, which serves as a reservoir. The sampling cylinder is equipped with a pressure regulator and is connected to the rest of the GHS via a pneumatic control valve. The sampling cylinder is cooled by immersion in a Dewar filled with liquid nitrogen (LN_2) at a temperature of around 78 K. The Xe gas condensates at 133 K so that the Xe liquefies in the reservoir and is slowly removed from the ELOSS vessel and the GHS tubes. This technical solution allows one to achieve a recovery yield of around 99% of the Xe in a short time (estimated to be <60 min). Once the recovery is complete, the reservoir is removed from the Dewar and returns to ambient temperature. At that point, the Xe in the reservoir returns to the gas phase and can be reinjected into the ELOSS detector through the supply line. The primary purpose of the recovery system is to recuperate the expensive Xe gas to be reused in successive ELOSS operations.

Electronegative impurities, such as water or oxygen, absorb scintillation light and reduce the number of ionization electrons through capture (attachment). Impurities are constantly outgassing into the Xe from all components of the detector and the gas

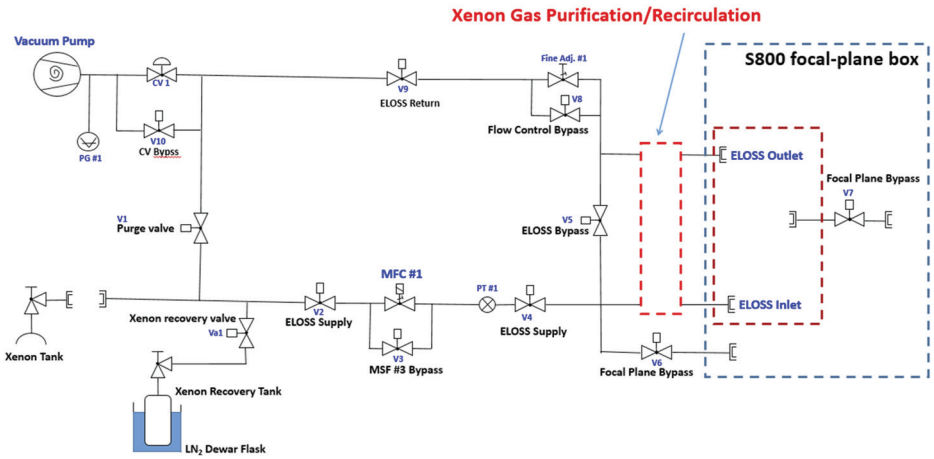

FIG. 3. Schematic drawing of the gas handling system for the operation of the ELOSS detector. The schematic diagram of the purification/recirculation system is shown in Fig. 4.

handling system. The purity of the Xe in the detector mainly depends on two variables: the outgassing rate of impurities (O_2, N_2, CO_2, CO, H_2O, etc.) from the surfaces of the detector components in contact with the Xe, and the efficiency of the purification system, which is related to its recirculation rate and the efficiency of the gas purifier. If the recirculation rate is sufficiently high and materials used for the various mechanical support of the detector components have low outgassing, the amount of impurities is sufficiently reduced to attain a high scintillation yield.

The ELOSS GHS includes a continuous recirculation loop (Fig. 4) through a GateKeeper gas purifier (model GPU 15). A miniature dry floating scroll vacuum pump (Scroll Labs, model SVF-5[21]) drives the gas recirculation at a flow rate in the range of 30–50 SCCM, which is regulated by means of a fine adjustment valve. The rate is measured in real time using a digital flowmeter (Alicat, model MW-5SLPM-D). Reduction of the impurities to a sub-ppb level is achieved after a few hours of closed-loop recirculation. The continuous flow of gas across the effective volume of the detector will also ensure good radiation hardness through the replenishment of the detector medium.

A dedicated system architecture based on programmable logic controllers (PLCs) is used for guiding all of the system states between the various GHS operational cycles, including the automatic control of pneumatic valves, computer-controlled safety procedures for the detector evacuation, the recirculation for gas purification, and the gas recovery system. Pumps, mass flow controllers, and diagnostic sensors (pressures, temperatures, etc.) are regulated by this system as well.

C. The data acquisition system (DAQ)

PMT signals, extracted from the AC decoupling capacitor in the decoupler box, are processed by a fast, high-resolution time and amplitude digitizer (Mesytec, model MDPP-32-QDC[22]). The 32-channel MDPP-32-QDC comprises an adjustable low-noise amplifier, a zero-crossing detector, a fast charge-integrating Analog-to-Digital Converter (ADC) with two different integration times for pulse-shape discrimination, and a Time-to-Digital Converter (TDC) for timing measurements. To achieve a high dynamic range and allow for the use of various types of pre-amplifiers, the MDPP-32 is equipped with a sophisticated low-noise input stage, and the amplification gain can be set from 1 to 250 in steps of 1%. The system is thus very flexible and suitable for analyzing the ELOSS data.

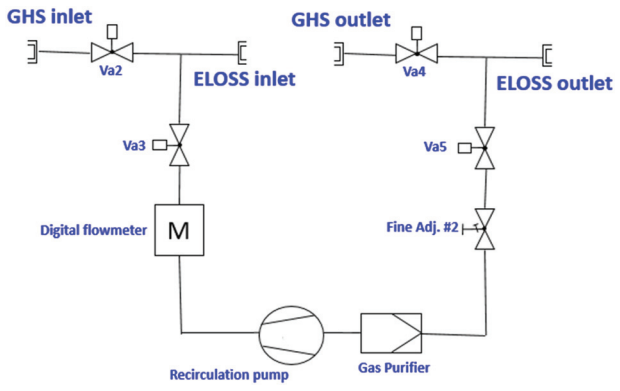

FIG. 4. Details of the purification/recirculation system to reduce impurities in the Xe.

A typical physics event recorded by the ELOSS detector consists of time-correlated signals from all 120 PMTs, which correspond from a few tens to a few thousand photoelectrons. The PMT signal pulse-height depends on several factors: the position of the impinging isotope on the detector area, particle trajectory, atomic number of the incident beam particle, pressure of the filling gas, and sensitivity of the PMTs. To avoid saturation, the bias voltage and thus the gains of the PMTs are adjusted accordingly. Simultaneous measurements of the time and amplitude are recorded for each PMT. As the decay time constants of the Xe–Xe dimer, singlet and triplet states, are reported to be ~5 and ~30 ns, respectively,[8] the typical MDPP-32-QDC integration time is set to 200 ns. When the ELOSS is operated in stimulated electroluminescence mode, the integration time is set to 3 μs to allow all the light created during the electron's drift time to be collected.

The energy-loss is computed as the average of the integrated light charge measured from all the PMTs and corrected for the position of the particle. The position and trajectory of the particles are computed using the S800 tracking system measurements which are positioned upstream of the ELOSS detector. Instead, the timing information from ELOSS is computed by averaging the time measurements obtained from the PMTs of the first sector only (the first to be crossed by the impinging beam particle). An additional correction of the timing data may be needed to take into account the position of the impinging particle. A moderate (a few mm) localization capability can also be obtained by processing the center of the gravity of the light distribution sensed by the PMT arrays in each sector.

The ELOSS DAQ is integrated within the existing FRIB S800 spectrograph DAQ framework, which allows one to synchronize and merge the data streams coming from the various detector systems of the S800 focal plane into a single data stream for event-by-event corrected analysis.

III. DESIGN STUDIES

A. Selection of the photosensor technology

The market nowadays offers a broad assortment of diverse photodetector technologies for large area coverings with extremely high performance, including high detection efficiency, a wide selection of spectral responses, excellent time resolution, a choice of various sizes, and high-rate capability. Several commercially available options with sensitivity in the deep ultraviolet (DUV) region include a high-granularity array of SiPMs,[23,24] large-area avalanche photomultiplier,[25,26] standard vacuum PMTs, Multi-Channel Plate PMTs (MCP-PMTs),[27] and position-sensitive gas photomultiplier equipped with a CsI PC,[28] but for which more development effort is generally required.

Three examples out of the many detector configurations that have been investigated are schematically illustrated in Fig. 5. These include arrays of Hamamatsu R8520-406 PMTs comprising a total of 120 units (a), arrays of Hamamatsu R12699-406 PMTs[29] comprising a total of 30 units (b), and an array of large-area MCP-PMT with a total of 6 units (c).

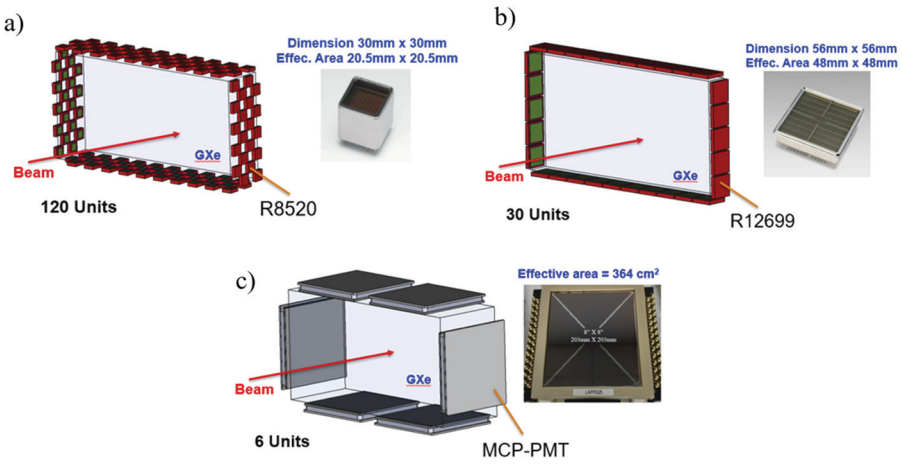

FIG. 5. Examples of different configurations studied for the design of the ELOSS optical readout: (a) chess-board-like arrays of R8520-406 PMTs displayed in four sectors; (b) arrays of R12699-406 PMTs in a single sector; and (c) uniformly spaced, large-area MCP-PMTs.

The arrangement of the sensors in each configuration was chosen to obtain the highest light collection efficiency for that configuration. The system with the R8520-406 PMTs, described in detail above (Sec. II A), was modeled by arranging the devices in a chess-board-like pattern within four equally spaced sectors [Fig. 5(a)].

The R12699-406 PMT has a square 2 in. multi-anode photosensitive area, together with a higher photocathode coverage of 75% as opposed to ~58% for R8520-406. The spectral response and photon detection efficiency (PDE) of the R12699-406 and R8520-406 are similar. Because of their large area, the R12699 PMTs readout was modeled by displaying the PMTs in a single sector [Fig. 5(b)]. This configuration resulted in a large straggling of the energy deposited by the impinging particle, due to the short track in the Xe volume, which leads to poor energy resolution. To reduce the energy straggling, other arrangements have been investigated based on the same number of devices (same cost). However, all of them lead to a substantial loss of light collection efficiency and poor response uniformity. Geometries with a thick effective volume and a large number of R12699 PMTs to recover part of the light collection efficiency would be unaffordable.

Finally, we have modeled six units of MCP-PMT detectors, each of 300 × 300 mm^2 area coverage, uniformly positioned along the four sides of the Xe effective volume [Fig. 5(c)]. Commercially available, large-area MCP-PMT can be coupled to a CsI-based PC, reaching quantum efficiency of around 25% for 178 nm wavelength and an open area ratio of around 80% so that the effective photon detection efficiency is around 18%. These devices are extremely fast (<20 ps, σ) and can provide localization capability if equipped with a suitable segmented anode plane and a dedicated multi-input DAQ.[30] However, because of the large area, the MCP-PMTs will be completely flooded by the large amount of scintillation light that reaches their PCs, with an overwhelming increase in the output current. This will eventually result in a loss of linearity and other saturation effects with a corresponding limitation of the overall ELOSS counting rate capability.

The evaluation performance of the different systems was computed through a series of systematic Monte Carlo simulations based on Geant4.[31,32] The modeling of the detector and the irradiation conditions allows for the design of the mechanical components, its operational conditions (gas pressure, beam particle, and energy), the track of the beam particle through the detector's effective volume, the physics process of the scintillation mechanism, and the efficiency of the photosensors under consideration.

Figure 6(b) illustrates an example of the PID obtained from the Monte Carlo computation of the R8520-406 readout configuration

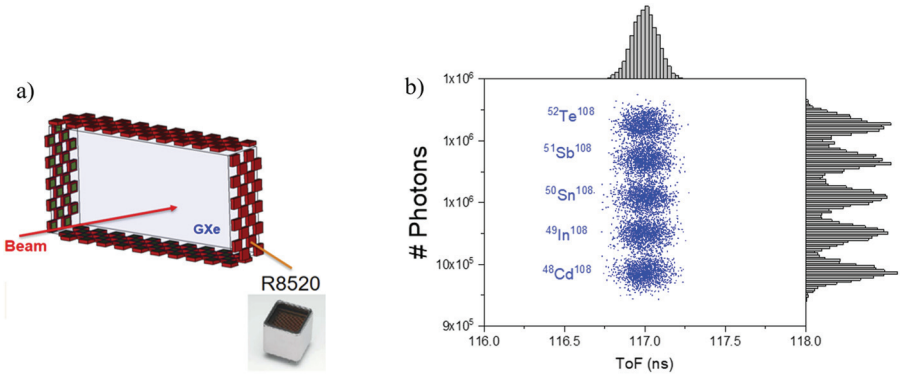

FIG. 6. Example of PID capability [number of detector photons as a function of the TOF (b)] computed by Monte Carlo (GEANT4) simulations assuming the ELOSS detector is equipped with the R8520-406 PMT's based optical readout as schematically illustrated in (a).

[schematically illustrated in (a)]. The simulation follows the track of five different types of fully stripped isotopes, 1500 primary particles per type, with an energy of 100 MeV/u. The different isotopes, from $^{108}Cd^{48+}$ to $^{108}Te^{52+}$, have the same mass number (A) but with a progressive increase in atomic number (Z). The Xe in the ELOSS was set at a pressure of 1 atm. In these conditions, the light collection efficiency was 16.3%, and the system achieved an energy resolution of 1.2% σ, which corresponds to a ΔZ/Z resolution of 0.62. Once position corrections have been introduced, and assuming a Xe pressure of 1.3 atm, energy resolutions below 0.6% σ can be achieved, which correspond to ΔZ/Z resolutions below 0.4. The TOF measurement was computed by the arrival time of the scintillation photons on the R8520-406 PMT arrays which were convoluted with an 80 ps time spread due to the DAQ time resolution.

The configuration based on the R8520-406 PMTs was eventually selected as a readout for the ELOSS detector as a good compromise between performance parameters (energy resolution, counting rate, and timing) and cost, which takes into account the number of individual detectors, the related number of DAQ channels, and other interfaces/equipment (e.g., cables and HV power supplies).

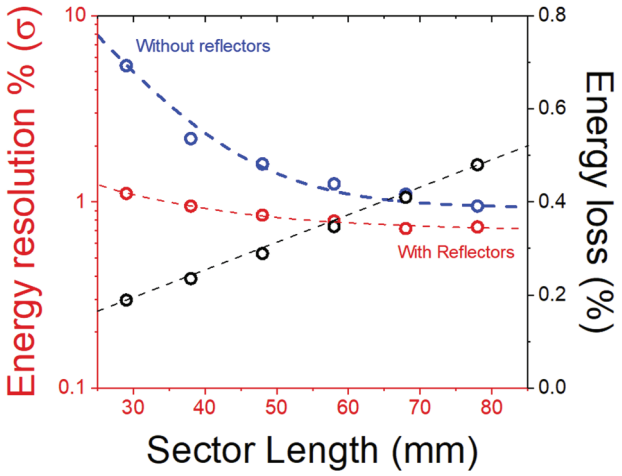

FIG. 8. Expected ELOSS energy resolution (%, σ) as a function of the distance between PMT arrays (sector length) and computed from the two geometries—with (red graph) and without (blue graph) reflective foils. The energy lost by the beam particle ($^{108}Sn^{+50}$) in the ELOSS volume (black graph) is also shown.

B. Optimization of the array's thickness

The ELOSS detector can operate in two different modes: primary scintillation and electroluminescence modes. The two approaches have different requirements. The light yield in the primary scintillation mode is the highest when no electric field is present across the effective volume. The gas volume can be either fully open [Fig. 7(a)], so that each PMT in the readout has a large solid angle of view, or segmented by reflectors [Fig. 7(b)] that drive the scintillation light created in the small gas gap toward the optical readout.

In contrast, the electroluminescence mode requires an electric field capable of drifting the ionization electrons across the gas gap and producing secondary Xe excitations. The electric field strength should be above the Xe excitation threshold but lower than the gas ionization threshold to avoid degradation of the energy resolution due to the avalanche process. To produce the electric field across the Xe volume, suitable electrodes must be introduced into the volume. A short distance between the electrode foils keeps the voltage difference small, so the probability of sporadic discharge and secondary undesired effects is small. However, a larger gas gap allows the collection of a large amount of light. The electrode foils can function as reflectors as well. The presence of electrode/reflector foils has the advantage that it allows both modes of operation, but the distance between the electrode/reflector foils needs to be optimized.

A dedicated Monte Carlo simulation study was carried out to investigate the effects of the reflectors' presence on the light collection efficiency, assuming a primary scintillation mode of operation. The simulation also serves to compute the optimal thickness of the whole ELOSS scintillating volume as well as the distance between two bordering reflectors.

Figure 8 illustrates the expected energy resolution (%, σ) measured by the optical readout as a function of the distance between PMT arrays (sector length) and computed from the two geometries—with (red graph) and without (blue graph) reflective foils. The ELOSS was modeled as a volume filled with Xe at 1 atm of different sizes, where the Xe primary scintillation yield was set to 13 ph/keV. The reflective/electrode surfaces were modeled as thin (0.5 mg/cm^2) polypropylene foils with a 150 nm layer of Al evaporated on both sides. The reflectivity of the Al layer was conservatively set to a value of 80%.[33] Figure 8 also shows the energy lost by the beam particle ($^{108}Sn^{+50}$) in the ELOSS volume (black graph), assuming the impinging isotopes have an initial energy of 80 MeV/u.

As shown by Fig. 8, longer tracks provide a better energy resolution, thanks to a larger amount of energy deposited by the impinging particle in the Xe volume. The effective improvement of energy resolution for thicker sections was more pronounced in the case of the open volume configuration. The presence of the reflectors allows a

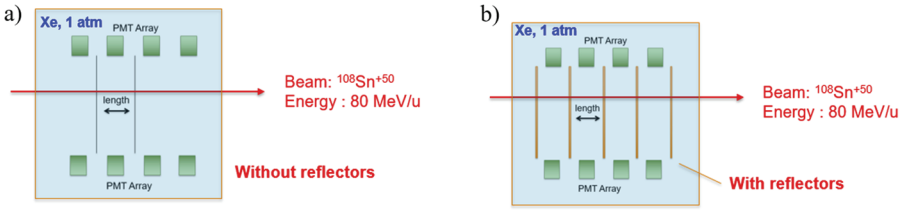

FIG. 7. Schematic drawing of the two possible ELOSS geometries: open volume (a) and segmented volume with reflector (b).

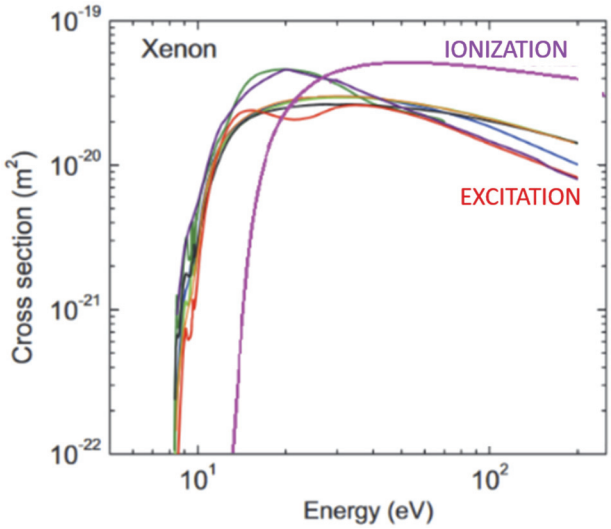

FIG. 9. Xenon electron-impact cross sections.

better collection of the scintillation photons and leads to a several times lower energy resolution, with small effects from the length of the gas gap.

However, a longer distance between the electrode/reflective foils will require a much larger bias voltage when the ELOSS is operated in electroluminescence mode. High electric fields are needed to overcome the secondary scintillation threshold [for Xe is roughly 0.8 (kV/cm)/bar[13]]. Too high of a bias voltage applied to the fragile foils may result in an unstable operational condition, causing sporadic, harmful discharges and a high probability of damaging various detector components. To preserve the possibility to operate the ELOSS detector in electroluminescence mode when high yield is required, the gas gap between the electrode/reflective foils has been chosen to be 47 mm, as a compromise between a reasonable low voltage operation and an acceptable energy resolution.

C. Selection of Xe as filling media

Pure noble gases are efficient scintillating media. While argon (Ar), neon (Ne), and krypton (Kr) could, in principle, be good media for ELOSS operation, they are inferior to Xe because the luminescence spectrum of Xe peaks at a much higher wavelength (178 nm) as compared to the other noble gases (e.g., the excimer spectra of Ar and Kr peak at 120 and 148 nm, respectively).[8,34] As a result, the Xe emission is more easily detected with commercially available photon-sensor devices at a reasonable detection efficiency. Xe also has a high primary scintillation yield (13.8 photon/keV) among the noble gases and is rather dense (5.761 kg/m^3 at standard operating temperature and pressure). In addition, the Xe scintillation process is quite fast—the decay time of the fast component is around 5 ns while the slow component has a decay time of around 30 ns.[8]

High scintillation light yield in ionization mode can be stimulated (electroluminescence) by electric field strengths below the threshold of the gas avalanche.[35] The reason for the presence of a window in the electric field strength, for which the drifting electrons only excite the Xe atoms without producing an avalanche process, is illustrated in Fig. 9. It depicts the excitation and ionization cross sections vs electron energy for the Xe gas. The Vacuum Ultra-Violet (VUV) emitting electron-impact excitation processes in Xe have a threshold E^* of around 8.5 eV, which is lower than the ionization threshold E_I of 10.5 eV. If the electrons are accelerated to energies slightly above E_I (corresponding to the end of the ionization region), the excitation probability will be much higher than the ionization probability, leading to a large production of scintillation photons along their tracks without triggering a significant charge multiplication.

High scintillation yields at a relevant (detectable) wavelength range can also be obtained from noble gases with small admixtures of certain impurities that shift the wavelength to a more suitable range.

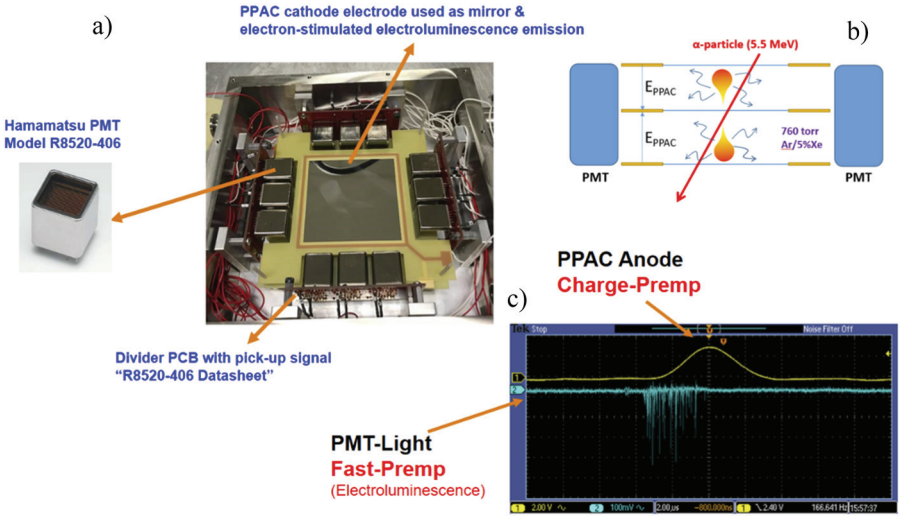

FIG. 10. (a) Photograph of the ELOSS prototype used to test the electroluminescence mode of operation is schematically illustrated in (b). (c) An oscilloscope snapshot with the comparison between charge and light signals recorded by the detector when irradiated by 5.5 MeV alpha-particles.

In fact, in the presence of a tiny amount of certain impurities, the excimer emission will be suppressed, whereas the emission of the impurities' molecules will dominate. The primary noble-gas component (i.e., Xe or Ar) acts as a detector medium while the impurities act as wavelength-shifters. Examples of such impurities to be added to noble gases are TEA, TMEA, N_2, CF_4, CO_2, CH_4, etc.

The operational principle of ELOSS in electroluminescence mode was investigated with a small-area ELOSS prototype [Fig. 10(a)]. Figure 10(c) illustrates an oscilloscope snapshot of electroluminescence and charge signals obtained from a small-area ELOSS prototype operated in Ar/Xe at 760 Torr. The detector comprises two parallel-plate chambers with a common anode foil at ground potential, from which the charge signals are extracted and processed by a charge-sensitive preamplifier [Fig. 10(b)]. The two external electrodes were biased with voltages of around 1500 V. The optical readout consisted of arrays of Hamamatsu R8520-406, arranged along the four sides of the detector's effective volume. The detector was irradiated with a collimated 5.5 MeV alpha-particle source (^{241}Am).

While the electroluminescence mode of operation allows one to achieve higher scintillation yield, the light is produced on a much longer time scale (μs as opposed to a few hundred ns). The operation of ELOSS in this mode needs to be driven by compromising the counting rate, $\Delta Z/Z$ resolution, and pressure and type of scintillating gas mixture. Operation of the ELOSS detector in electroluminescence mode with different gas mixtures and the related performance evaluation in terms of $\Delta Z/Z$ resolution will be reported elsewhere.[36]

IV. CONCLUSIONS

The design and construction of the novel ELOSS detector, which is intended for Z-identification based on energy-loss measurement at the focal plane of the S800 spectrograph, have been described. ELOSS is a cutting-edge experimental device based on an innovative, fast optical readout scheme which offers several noteworthy technical advantages compared to conventional charge readout systems:

- An improved energy-loss resolution, expected to be about 0.6% σ instead of >1% σ. Unlike conventional ICs, which are characterized by large electrode foils with significant induced capacitive noise, the optical readout of ELOSS is completely decoupled from the drift region. The small detector capacitance of the PMT-based readout, together with the low limit of the PMT threshold (down to single-photon detection efficiency), allows ELOSS to reach larger signal-to-noise ratios and consequently a better resolving power. The detector can be optionally operated in electroluminescence mode, which provides a high stimulated scintillation yield and, thus potentially, a higher energy resolution which is mostly determined by the statistical fluctuation of the energy loss in the detector medium. The large dynamic range of the detector, which is achieved by adjusting the pressure of the filling gas, leads to a better intrinsic energy resolution of ELOSS and extends to the Z-identification to elements with atomic number $Z > 50$.
- An improved rate capability (>50 kHz compared to 5 kHz at present): the ELOSS concept, based on recording the prompt electroluminescence emission, is a much faster detector as compared to the conventional IC. In the case of Xe gas, more than 90% of the scintillation photons are emitted within 100 ns, which provides an extremely sharp signal rise time. For the stimulated scintillation mode of operation, the photon emission is mainly dictated by the time needed by the ionization electrons to reach the electrode foil (a few μs). To avoid signal saturation and loss of linearity, the gain of the PMTs and the light yield (by changing gas pressure) produced in the ELOSS volume can be adjusted accordingly. The upper limit of the counting rate is then solely imposed by the performance of the DAQ electronics, which will be able to record beam rates up to around 50 kHz in trigger mode.
- Timing capability: the timing performance of ELOSS is affected by several parameters, including the PMT transit time spread (TTS), the number of detected photoelectrons, and the scintillation decay time. However, all these factors are negligible compared to the channel-to-channel time response of the Mesytec MDPP-32-QDC, being around 80 ps, which dominates the time resolution of the full detector system. The time response of the PMTs also depends on the position of the beam particle, so the overall timing fluctuations over the full effective area are estimated to be <150 ps FWHM, compared to no useable timing information provided by a conventional IC. This performance is comparable to what can be achieved with a thin plastic scintillator.
- Localization capability: preliminary Monte Carlo simulations indicate that, by computing the center of gravity of the light distributions recorded in the various PMT arrays, a moderate localization capability of a few mm can be achieved. This may be very helpful for experiments in which more than one particle per event is to be detected in the focal plane, and the drift chambers alone are not sufficient to disentangle the horizontal and vertical coordinates of the two tracks.

The advance in the focal plane detector performance largely benefits the scientific programs at the S800 spectrograph, which capitalize on the high luminosity of ~100 MeV/u rare isotope beams with thick targets. The increased ΔE resolution and the order-of-magnitude increase in the maximum S800 focal plane rate provided by the ELOSS detector open up an entirely new region of the nuclear chart for nuclear structure and nuclear astrophysical studies, which is enabled also by the availability of heavier beams expected from FRIB. ELOSS also serves as a prototype for the development of PID technologies of other planned and future spectrometers, such as the high rigidity spectrometer.[4]

ACKNOWLEDGMENTS

This work was supported by the NSF-MRI under Grant No. PHY-2017986.

AUTHOR DECLARATIONS

Conflict of Interest

The authors have no conflicts to disclose.

Author Contributions

M. Cortesi: Conceptualization (lead); Data curation (lead); Formal analysis (equal); Funding acquisition (equal); Investigation (lead); Project administration (lead); Supervision (equal); Writing – original draft (lead). **S. Dziubinski**: Conceptualization (equal); Data curation (equal); Formal analysis (equal); Investigation (equal); Methodology (equal); Writing – review & editing (equal). **A. Gade**: Conceptualization (equal); Data curation (equal); Funding acquisition (equal); Project administration (equal); Supervision (equal); Writing – review & editing (equal). **R. Zegers**: Conceptualization (equal); Data curation (equal); Funding acquisition (equal); Project administration (equal); Supervision (equal); Writing – review & editing (equal). **J. Pereira**: Conceptualization (equal); Data curation (equal); Methodology (equal); Supervision (equal); Validation (equal); Writing – review & editing (equal). **J. Asciutto**: Conceptualization (equal); Data curation (equal); Investigation (equal); Methodology (equal); Writing – review & editing (equal). **S. Lidia**: Conceptualization (equal); Data curation (equal); Funding acquisition (equal); Methodology (equal); Supervision (equal); Writing – review & editing (equal). **D. Bazin**: Conceptualization (equal); Data curation (equal); Methodology (equal); Supervision (equal); Writing – review & editing (equal).

DATA AVAILABILITY

The data that support the findings of this study are available from the corresponding author upon request.

REFERENCES

[1] D. Bazin, J. A. Caggiano, B. M. Sherrill, J. Yurkon, and A. Zeller, Nucl. Instrum. Methods Phys. Res., Sect. B **204**, 629 (2003).

[2] Z. Meisel and S. George, Int. J. Mass Spectrom. **349–350**, 145 (2013).

[3] N. Frank, A. Schiller, D. Bazin, W. A. Peters, and M. Thoennessen, Nucl. Instrum. Methods Phys. Res., Sect. A **580**, 1478 (2007).

[4] S. Noji, R. G. T. Zegers, G. P. A. Berg, A. M. Amthor, T. Baumann, D. Bazin, E. E. Burkhardt, M. Cortesi, J. C. DeKamp, M. Hausmann, M. Portillo, D. H. Potterveld, B. M. Sherrill, A. Stolz, O. B. Tarasov, and R. C. York, Nucl. Instrum. Methods Phys. Res., Sect. A **1045**, 167548 (2022).

[5] J. Yurkon, D. Bazin, W. Benenson, D. J. Morrissey, B. M. Sherrill, D. Swan, and R. Swanson, Nucl. Instrum. Methods Phys. Res., Sect. A **422**, 291 (1999).

[6] K. Y. Chae, S. Ahn, D. W. Bardayan, K. A. Chipps, B. Manning, S. D. Pain, W. A. Peters, K. T. Schmitt, M. S. Smith, and S. Y. Strauss, Nucl. Instrum. Methods Phys. Res., Sect. A **751**, 6 (2014).

[7] M. Cortesi, J. Pereira, D. Bazin, Y. Ayyad, G. Cerizza, R. Fox, and R. G. T. Zegers, J. Instrum. **15**, P03025 (2020).

[8] E. Aprile, A. E. Bolotnikov, A. I. Bolozdynya, and T. Doke, *Noble Gas Detectors* (John Wiley & Sons, 2007).

[9] M. Yang, A. Gatto, and N. Kaiser, Appl. Opt. **45**, 178 (2006).

[10] Fibre Glast Developments Corp. (https://www.fibreglast.com).

[11] Hexion SF 8024: Resin System 828 9552 (https://www.hexion.com).

[12] C. M. B. Monteiro, R. D. P. Mano, E. C. G. M. Barata, L. M. P. Fernandes, and E. D. C. Freitas, J. Instrum. **11**, C12079 (2016).

[13] D. González-Díaz, F. Monrabal, and S. Murphy, Nucl. Instrum. Methods Phys. Res., Sect. A **878**, 200 (2018).

[14] E. Nappi and V. Peskov, *Imaging Gaseous Detectors and Their Applications*, Science edition (John Wiley & Sons, 2013).

[15] Hamamatsu R8520-406 datasheet (https://www.hamamatsu.com/).

[16] S. Li, X. Chen, K. L. Giboni, G. Guo, X. Ji, Q. Lin, J. Liu, Y. Mao, K. Ni, X. Ren, A. Tan, M. Xiao, X. Xiao, and X. Zhou, J. Instrum. **11**, T02005 (2016).

[17] P. Chiggiato, *Proceedings of the 2017 CERN Accelerator School Course on Vacuum for Particle Accelerators* (Glumslov, Sweden, 2017), https://cas.web.cern.ch/previous-schools.

[18] Hamamatsu private communication.

[19] S. Dziubinki, M. Cortesi, and S. Lidia, "Calibration of the PMT-based optical readout of the ELOSS detector" (unpublished).

[20] X. Cao, X. Chen, Y. Chen, X. Cui, D. Fang, C. Fu, K. L. Giboni, H. Gong, G. Guo, M. He, J. Hu, X. Huang, X. Ji, Y. Ju, S. Li, Q. Lin, H. Liu, J. Liu, X. Liu, W. Lorenzon, Y. Ma, Y. Mao, K. Ni, K. Pushkin, X. Ren, M. Schubnell, M. Shen, Y. Shi, S. Stephenson, A. Tan, G. Tarlé, H. Wang, J. Wang, M. Wang, X. Wang, Z. Wang, Y. Wei, S. Wu, M. Xiao, X. Xiao, P. Xie, T. Ye, Y. You, X. Zen, H. Zhang, T. Zhang, H. Zhao, L. Zhao, X. Zhou, and Z. Zhu, Sci. China: Phys., Mech. Astron. **57**, 1476 (2014).

[21] Scroll Labs Vacuum Pumps (https://www.scrolllabs.com).

[22] Mesytec - Detector Readout Systems (https://www.mesytec.com/).

[23] N. Yahlali, L. M. P. Fernandes, K. González, A. N. C. Garcia, and A. Soriano, J. Instrum. **8**, C01003 (2013).

[24] J. Adam, X. Bai, A. M. Baldini, E. Baracchini, C. Bemporad, G. Boca, P. W. Cattaneo, G. Cavoto, F. Cei, C. Cerri, M. Corbo, N. Curalli, A. De Bari, M. De Gerone, L. Del Frate, S. Doke, S. Dussoni, J. Egger, K. Fratini, Y. Fujii, L. Galli, S. Galeotti, G. Gallucci, F. Gatti, B. Golden, M. Grassi, A. Graziosi, D. N. Grigoriev, T. Haruyama, M. Hildebrandt, Y. Hisamatsu, F. Ignatov, T. Iwamoto, D. Kaneko, K. Kasami, P.-R. Kettle, B. I. Khazin, O. Kiselev, A. Korenchenko, N. Kravchuk, G. Lim, A. Maki, S. Mihara, W. Molzon, T. Mori, F. Morsani, D. Mzavia, R. Nardò, H. Natori, D. Nicolò, H. Nishiguchi, Y. Nishimura, W. Ootani, K. Ozone, M. Panareo, A. Papa, R. Pazzi, G. Piredda, A. Popov, F. Raffaelli, F. Renga, E. Ripiccini, S. Ritt, M. Rossella, R. Sawada, M. Schneebeli, F. Sergiampietri, G. Signorelli, S. Suzuki, F. Tenchini, C. Topchyan, Y. Uchiyama, R. Valle, C. Voena, F. Xiao, S. Yamada, S. Yamamoto, S. Yamashita, Yu. V. Yudin, and D. Zanello, Eur. Phys. J. C **73**, 2365 (2013).

[25] L. M. P. Fernandes, F. D. Amaro, A. Antognini, J. M. R. Cardoso, C. A. N. Conde, O. Huot, P. E. Knowles, F. Kottmann, J. A. M. Lopes, L. Ludhova, C. M. B. Monteiro, F. Mulhauser, R. Pohl, J. M. F. d. Santos, L. A. Schaller, D. Taqqu, and J. F. C. A. Veloso, J. Instrum. **2**, P08005 (2007).

[26] K. Ni, E. Aprile, D. Day, K. L. Giboni, J. A. M. Lopes, P. Majewski, and M. Yamashita, Nucl. Instrum. Methods Phys. Res., Sect. A **551**, 356 (2005).

[27] M. J. Minot, B. W. Adams, M. Aviles, J. L. Bond, T. Cremer, M. R. Foley, A. Lyashenko, M. A. Popecki, M. E. Stochaj, W. A. Worstell, M. J. Wetstein, J. W. Elam, A. U. Mane, O. H. W. Siegmund, C. Ertley, H. J. Frisch, A. Elagin, E. Angelico, and E. Spieglan, Nucl. Instrum. Methods Phys. Res., Sect. A **936**, 527 (2019).

[28] L. Arazi, A. E. C. Coimbra, E. Erdal, I. Israelashvili, M. L. Rappaport, S. Shchemelinin, D. Vartsky, J. M. F. dos Santos, and A. Breskin, arXiv:1508.00410 [Physics] (2015).

[29] Hamamatsu R12699-406 datasheet (https://www.hamamatsu.com/).

[30] G. R. Jocher, M. J. Wetstein, B. Adams, K. Nishimura, and S. M. Usman, Nucl. Instrum. Methods Phys. Res., Sect. A **822**, 25 (2016).

[31] S. Agostinelli, J. Allison, K. Amako, J. Apostolakis, H. Araujo, P. Arce, M. Asai, D. Axen, S. Banerjee, G. Barrand, F. Behner, L. Bellagamba, J. Boudreau, L. Broglia, A. Brunengo, H. Burkhardt, S. Chauvie, J. Chuma, R. Chytracek, G. Cooperman, G. Cosmo, P. Degtyarenko, A. Dell'Acqua, G. Depaola, D. Dietrich, R. Enami, A. Feliciello, C. Ferguson, H. Fesefeldt, G. Folger, F. Foppiano, A. Forti, S. Garelli, S. Giani, R. Giannitrapani, D. Gibin, J. J. Gómez Cadenas, I. González, G. Gracia Abril, G. Greeniaus, W. Greiner, V. Grichine, A. Grossheim, S. Guatelli, P. Gumplinger, R. Hamatsu, K. Hashimoto, H. Hasui, A. Heikkinen, A. Howard, V. Ivanchenko, A. Johnson, F. W. Jones, J. Kallenbach, N. Kanaya, M. Kawabata, Y. Kawabata, M. Kawaguti, S. Kelner, P. Kent, A. Kimura, T. Kodama, R. Kokoulin, M. Kossov, H. Kurashige, E. Lamanna, T. Lampén, V. Lara, V. Lefebure, F. Lei, M. Liendl, W. Lockman, F. Longo, S. Magni, M. Maire, E. Medernach, K. Minamimoto, P. Mora de Freitas, Y. Morita, K. Murakami, M. Nagamatu, R. Nartallo, P. Nieminen, T. Nishimura, K. Ohtsubo, M. Okamura, S. O'Neale, Y. Oohata, K. Paech, J. Perl, A. Pfeiffer, M. G. Pia, F. Ranjard, A. Rybin, S. Sadilov, E. Di Salvo, G. Santin, T. Sasaki, N. Savvas, Y. Sawada, S. Scherer, S. Sei, V. Sirotenko, D. Smith, N. Starkov, H. Stoecker, J. Sulkimo, M. Takahata, S. Tanaka, E. Tcherniaev, E. Safai Tehrani, M. Tropeano, P. Truscott, H. Uno, L. Urban, P. Urban, M. Verderi, A. Walkden, W. Wander, H. Weber, J. P. Wellisch,

T. Wenaus, D. C. Williams, D. Wright, T. Yamada, H. Yoshida, and D. Zschiesche, Nucl. Instrum. Methods Phys. Res., Sect. A **506**, 250 (2003).
[32]J. Allison, K. Amako, J. Apostolakis, H. Araujo, P. Arce Dubois, M. Asai, G. Barrand, R. Capra, S. Chauvie, R. Chytracek, G. A. P. Cirrone, G. Cooperman, G. Cosmo, G. Cuttone, G. G. Daquino, M. Donszelmann, M. Dressel, G. Folger, F. Foppiano, J. Generowicz, V. Grichine, S. Guatelli, P. Gumplinger, A. Heikkinen, I. Hrivnacova, A. Howard, S. Incerti, V. Ivanchenko, T. Johnson, F. Jones, T. Koi, R. Kokoulin, M. Kossov, H. Kurashige, V. Lara, S. Larsson, F. Lei, O. Link, F. Longo, M. Maire, A. Mantero, B. Mascialino, I. McLaren, P. Mendez Lorenzo, K. Minamimoto, K. Murakami, P. Nieminen, L. Pandola, S. Parlati, L. Peralta, J. Perl, A. Pfeiffer, M. G. Pia, A. Ribon, P. Rodrigues, G. Russo, S. Sadilov, G. Santin, T. Sasaki, D. Smith, N. Starkov, S. Tanaka, E. Tcherniaev, B. Tome, A. Trindade, P. Truscott, L. Urban, M. Verderi, A. Walkden, J. P. Wellisch, D. C. Williams, D. Wright, and H. Yoshida, IEEE Trans. Nucl. Sci. **53**, 270 (2006).
[33]S. Wilbrandt, O. Stenzel, H. Nakamura, D. Wulff-Molder, A. Duparré, and N. Kaiser, Appl. Opt. **53**, A125 (2014).
[34]C. M. B. Monteiro, L. M. P. Fernandes, J. A. M. Lopes, L. C. C. Coelho, J. F. C. A. Veloso, J. M. F. d. Santos, K. Giboni, and E. Aprile, J. Instrum. **2**, P05001 (2007).
[35]L. M. P. Fernandes, E. D. C. Freitas, M. Ball, J. J. Gómez-Cadenas, C. M. B. Monteiro, N. Yahlali, D. Nygren, and J. M. F. d. Santos, J. Instrum. **5**, P09006 (2010).
[36]S. Dziubinki, M. Cortesi, and S. Lidia, "Test of the ELOSS detector with fast, rare isotope beam" (unpublished).